AIAA JOURNAL
Vol. 41, No. 9, September 2003

Wall Pressure Fluctuations in a Turbulent Boundary Layer After Blowing or Suction

Joongnyon Kim,* Kyoungyoun Kim,* and Hyung Jin Sung†
Korea Advanced Institute of Science and Technology, Daejon 305-701, Republic of Korea

A direct numerical simulation of a spatially developing turbulent boundary layer is performed to examine the characteristics of wall pressure fluctuations after the sudden application of wall blowing or suction. The uniform blowing or suction is given by the wall-normal velocity through a spanwise slot at the wall. The response of wall pressure fluctuations to uniform blowing or suction is analyzed by computing the turbulence statistics and frequency spectra. It is found that wall pressure fluctuations are more affected by blowing than by suction. The large elongated structure of wall pressure fluctuations is observed near the maximum location of $(p_w)_{\mathrm{rms}}$ for blowing. The convection velocities for blowing increase with increasing the streamwise location after the slot. For both blowing and suction, the small scale of wall pressure fluctuations reacts in a short downstream distance to the spanwise slot, whereas the large scale recovers slowly farther downstream.

Nomenclature

C_f	=	skin-friction coefficient
C_p	=	mean wall pressure coefficient
k_z	=	spanwise wave number
q_∞	=	reference dynamic pressure, $\rho U_\infty^2/2$
Re_θ	=	Reynolds number based on U_∞ and θ_0, $U_\infty\theta/\nu$
R_{pp}	=	two-point correlation of wall pressure flcutuations
U_∞	=	freestream velocity
u_τ	=	friction velocity
v_w	=	magnitude of blowing or suction
θ_0	=	inlet momentum thickness
$\Phi(k_z, \omega; x)$	=	power spectral density of wall pressure fluctuations
ω	=	frequency

Superscripts and Subscripts

rms	=	root mean square value
w	=	values at the wall
$'$	=	fluctuating component
$+$	=	normalized by u_τ and ν
$*$	=	complex conjugate
$\langle\ \rangle$	=	statistically averaged in time and the spanwise direction

I. Introduction

WALL pressure fluctuations in a turbulent boundary layer are of prime importance in many engineering applications involving flow-induced vibration, aircraft cabin noise, and hydroacoustics of underwater vehicles. Wave-number-frequency spectra of wall pressure fluctuations are required as the forcing input function for structural models of flow-induced sound and vibration.[1] Wall pressure fluctuations at a local point in a turbulent boundary layer are coupled with global unsteadiness of associated flow structures. In addition, the generation of wall pressure fluctuations is governed by the dynamics of velocity fluctuations throughout the entire boundary layer through a Poisson's equation.

A literature survey reveals that most experimental and computational accounts of wall pressure fluctuations have been focused on equilibrium turbulent boundary layers over flat plates or inside channels. The first measurement of wall pressure fluctuations was made in a turbulent boundary layer over a flat plate by Willmarth.[2] He found that the ratio of rms wall pressure to dynamic pressure was approximately 0.0035. Bull[3] observed that wall pressure field has a structure produced by pressure sources with a wide range of convection velocities. A comprehensive overview of the role of wall pressure fluctuations was complied by Willmarth.[4] Recently, the statistical and spectral features of wall pressure fluctuations were obtained by direct numerical simulations[5] and by measurements with multiarrayed pressure transducers.[6]

Relations of wall pressure fluctuations to near-wall coherent structures in equilibrium turbulent boundary layers have also received extensive investigation. By use of conditional average techniques, the velocity field structures related to high-amplitude wall pressure events were obtained experimentally.[7,8] It was found that the shear layer structures in the buffer region are responsible for the generation of high-amplitude wall pressure peaks. To study the structure of pressure fluctuations in turbulent channel flow, Kim[9] decomposed the pressure into the rapid, slow, and wall parts and analyzed their contributions to various statistical quantities. The relationship between wall pressure fluctuations and streamwise vortices was examined by Kim et al.[10] They found that the generation of wall pressure fluctuations is closely linked with upstream streamwise vortices and turbulent kinetic energy production. In an effort to see the effects of pressure gradient and separation on the characteristics of wall pressure fluctuations, space–time correlation and frequency spectra of wall pressure fluctuations obtained from direct numerical simulation were examined by Na and Moin.[11] They found that large two-dimensional roller-type structures are present inside the separation bubble. Recently, Lee and Sung[12,13] made a multiple-arrayed measurement of wall pressure fluctuations in a separated and reattaching flow over a backward-facing step. They found by using unsteady wavelet analysis of wall pressure fluctuations that there exist two modes of shed vortices.

Wall blowing or suction through a spanwise slot in a turbulent boundary layer has been frequently employed due to its potential possibility for turbulence control. Many direct numerical simulations were performed for testing the wall blowing or suction in a turbulent channel[14] and boundary-layer flows.[15,16] It is known that wall blowing gives rise to an upward shift in the mean velocity logarithmic law, whereas a downward shift of the logarithmic velocity

Received 15 May 2002; revision received 19 April 2003; accepted for publication 19 April 2003.

*Ph.D. Student, Department of Mechanical Engineering, 373-1, Gusong-dong, Yusong-gu.
†Professor, Department of Mechanical Engineering, 373-1, Gusong-dong, Yusong-gu; hjsung@kaist.ac.kr. Member AIAA.

profile results from wall suction. The turbulent stresses are activated by wall blowing and decreased in the suction case. The wall pressure fluctuations can be affected significantly by the application of wall blowing or suction.

The objective of the present study is, therefore, to investigate the effects of wall blowing or suction on the characteristics of wall pressure fluctuations. Toward this end, a direct numerical simulation (DNS) is made in a spatially developing turbulent boundary layer. The Reynolds number based on the inlet momentum thickness θ_0 and freestream velocity U_∞ is $Re_\theta = 300$. The uniform blowing or suction is given by the wall-normal velocity through a spanwise slot at the wall.[16] Main emphasis is placed on the response of wall pressure fluctuations to sudden uniform blowing or suction. Turbulence statistics and frequency spectra of wall pressure fluctuations are obtained using standard techniques for stochastic data.[11] To deduce the spatial structure of wall pressure fluctuations, two-point correlation coefficients and several instantaneous fields are examined. Convection nature of wall pressure fluctuations is presented in terms of spatio–temporal correlations and convection velocities. Based on the wealth of DNS data, the source terms of the Poisson's equation are analyzed to investigate the contribution of each term to wall pressure fluctuations.

II. Numerical Procedure

For an incompressible flow, the nondimensional governing equations are

$$\frac{\partial u_i}{\partial t} + \frac{\partial}{\partial x_j} u_i u_j = -\frac{\partial p}{\partial x_i} + \frac{1}{Re}\frac{\partial}{\partial x_j}\frac{\partial u_i}{\partial x_j}, \qquad i = 1, 2, 3 \quad (1)$$

$$\frac{\partial u_i}{\partial x_i} = 0 \quad (2)$$

where x_i are the Cartesian coordinates and u_i are the corresponding velocity components. All variables are nondimensionalized by a characteristic length and velocity scale, and Re is the Reynolds number.

The governing equations (1) and (2) are integrated in time by using a fully implicit decoupling method, proposed by Kim et al.[17] All terms are advanced with the Crank–Nicholson method in time, and they are resolved with the second-order central difference scheme in space. Based on a block lower–upper decomposition, both velocity–pressure decoupling and additional decoupling of the intermediate velocity components are achieved in conjunction with the approximate factorization.[17] The overall accuracy in time is second order without any modification of boundary conditions. Because the decoupled momentum equations are solved without iteration, the computational time is reduced significantly.

A simplified discretization of Eqs. (1) and (2) is made in a series of operations:

$$A\boldsymbol{u}^* = \boldsymbol{r} + \boldsymbol{mbc} \quad (3)$$

$$\Delta t DG\delta p = D\boldsymbol{u}^* - cbc \quad (4)$$

$$\boldsymbol{u}^{n+1} = \boldsymbol{u}^* - \Delta t G\delta p \quad (5)$$

where

$$A = (1/\Delta t)\{I + \Delta t[N - (1/2Re)L]\}$$

$$\boldsymbol{r} = (1/\Delta t)\boldsymbol{u}^n - Gp^{n-\frac{1}{2}} + (1/2Re)L\boldsymbol{u}^n$$

$$\delta p = p^{n+\frac{1}{2}} - p^{n-\frac{1}{2}}$$

L is the discrete Laplacian viscous operator, N is the linear discrete convective operator, G is the discrete gradient operator, and D is the discrete divergence operator, respectively. Δt is the time increment and the superscript n denotes the nth time step. The known velocities at the boundary have been imposed on $\boldsymbol{mbc}$ and cbc.

Next, the aforestated approximate factorization is further extended to the velocity components $\boldsymbol{u}^*$ in Eq. (3) by using the delta form $\delta\boldsymbol{u}^* = \boldsymbol{u}^* - \boldsymbol{u}^n$. Equation (3) is rewritten as

$$A\delta\boldsymbol{u}^* = -A\boldsymbol{u}^n + \boldsymbol{r} + \boldsymbol{mbc} \equiv \boldsymbol{R} \quad (6)$$

Here, the intermediate terms $\delta\boldsymbol{u}^*$ can be calculated separately in the following steps, which are exactly equivalent to Eq. (6) with new variables δu_1^{**} and δu_2^{**}:

$$1/\Delta t(I + \Delta t M_{11})\delta u_1^{**} = R_1 \quad (7)$$

$$1/\Delta t(I + \Delta t M_{22})\delta u_2^{**} = R_2 - M_{21}\delta u_1^{**} \quad (8)$$

$$1/\Delta t(I + \Delta t M_{33})\delta u_3^{**} = R_3 - M_{31}\delta u_1^{**} - M_{32}\delta u_2^{**} \quad (9)$$

$$\delta u_2^* = \delta u_2^{**} - \Delta t M_{23}\delta u_3^* \quad (10)$$

$$\delta u_1^* = \delta u_1^{**} - \Delta t M_{12}\delta u_2^* - \Delta t M_{13}\delta u_3^* \quad (11)$$

$$u_i^* = u_i^n + \delta u_i^*, \qquad (i = 1, 2, 3) \quad (12)$$

The coefficient matrices in Eqs. (7–9) are approximated with preserving the temporal second-order accuracy. A significant reduction in computing cost and memory is achieved by avoiding the inversion of a large sparse matrices. The overall numerical computation procedure is as follows:

1) Solve $\boldsymbol{u}^*$ from Eqs. (7–12) through the velocity decoupling procedure.

2) Solve δp from Eq. (4).

3) Obtain $\boldsymbol{u}^{n+1}$ from Eq. (5), which is a divergence-free vector field, and then one time step marching is finished.

A schematic diagram of the computational domain is shown in Fig. 1. Time-dependent turbulent inflow data are provided at the inlet based on the method by Lund et al.[18] This approach is to extract instantaneous planes of velocity data from an auxiliary simulation of the spatially developing turbulent boundary layer. A plane velocity field near the domain exit is modified by the rescaling procedure and reintroduced to the inlet of the computational domain in the inflow-generation simulation. The main simulation of the developing turbulent boundary layer is then carried out in the range $0 \le x \le 200\theta_0$. Details regarding the numerical procedure of inflow generation are available in Ref. 18. A convective boundary condition at the exit has the form $(\partial u_i/\partial t) + c(\partial u_i/\partial x) = 0$, where c is the local bulk velocity. The no-slip boundary condition is imposed at the solid wall, and the boundary conditions on the top surface of the computational domain are $u = U_\infty$ and $(\partial v/\partial y) = (\partial w/\partial y) = 0$. A periodic boundary condition is applied in the spanwise direction.

A spanwise slot for uniform blowing or suction is located from $x = 78.9\theta_0$ to $x = 87.5\theta_0$, where $x = 0$ corresponds to the inlet.[16] The slot width b is about $8.6\theta_0$. The magnitudes of uniform blowing, $v_w > 0$, or suction, $v_w < 0$, are 4.63% of the freestream velocity, U_∞, $|v_w| = 0.0463U_\infty$. The ratio of momentum flux gain/loss due to the blowing/suction and momentum flux of the incoming boundary layer, $\sigma = v_w b/U_\infty\theta_{\text{slot}}$, is 0.322, where θ_{slot} is the momentum thickness without blowing or suction at the slot location.[16]

The inlet Reynolds number based on the inlet momentum thickness θ_0 and freestream velocity U_∞ is $Re_\theta = 300$. The computational domain has dimensions $200\theta_0 \times 30\theta_0 \times 40\theta_0$ in the streamwise, wall-normal, and spanwise directions, respectively, which corresponds to $3200 \times 480 \times 640$ in wall units. The mesh contains

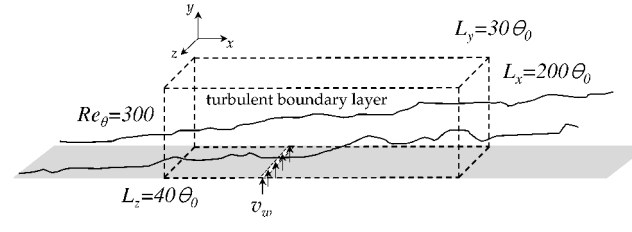

Fig. 1 Schematic diagram of the computational domain.

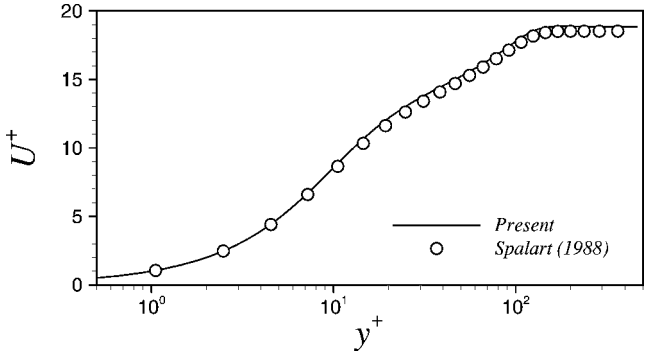

a) Mean velocity profile

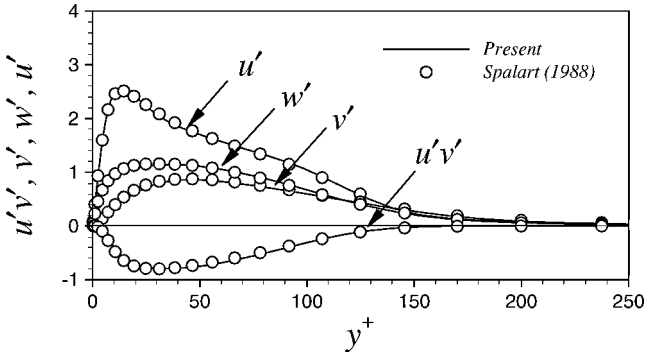

b) Turbulence intensities and Reynolds shear stress

Fig. 2 Comparison of turbulence statistics.

$257 \times 65 \times 129$ points in the streamwise, wall-normal, and spanwise directions, respectively. The grid resolution is $\Delta x^+ \cong 12.5$, $\Delta y^+_{\min} \cong 0.16$, $\Delta y^+_{\max} \cong 24.1$, and $\Delta z^+ \cong 5.0$ in wall units based on the inlet friction velocity u_τ. Uniform grids are deployed in the streamwise and spanwise directions, and a hyperbolic tangent distribution is used for grids in the wall-normal direction. The computational time step used is $\Delta t^+ = 0.25$, and the total averaging time to obtain the statistics is $T_{\text{av}} = 6250\nu/u_\tau^2$.

To ascertain the reliability and accuracy of the present numerical simulation, comparisons of the turbulence statistics with the DNS data of Spalart[19] are made and presented in Fig. 2. The mean velocity profile normalized by the friction velocity is shown in Fig. 2a, where $y^+ = yu_\tau/\nu$ and $U^+ = U/u_\tau$. Comparisons are extended to the turbulence intensities and Reynolds shear stress in Fig. 2b. The present results are in excellent agreement with the DNS data at the same Reynolds number $Re_\theta = 300$. This suggests that the resolution of the present study is sufficient to analyze the second-order turbulence statistics.

III. Results and Discussion

A. One-Point Statistics of Wall Pressure Fluctuations

Before proceeding further, it would be advantageous to see the variations of mean variables along the wall. Figure 3 shows the streamwise distribution of skin-friction, C_f, and wall pressure coefficients C_p. For uniform blowing, the skin-friction coefficient decreases rapidly near the slot. The adverse pressure gradient appears before and after the slot, whereas the favorable pressure gradient occurs above the slot. The opposite is observed for uniform suction. Overall characteristics of the mean wall variables are in good agreement with previous results.[15,16] It is known that when wall blowing is applied through a spanwise slot, streamwise vortices are lifted up with decreasing skin friction above the slot, whereas uniform suction diminishes turbulent fluctuations. However, the skin friction slightly increases in the downstream because of the increased turbulent motion by uniform blowing.[15]

The streamwise distribution of rms wall pressure fluctuations $(p_w)_{\text{rms}}$ normalized by a reference dynamic pressure $q_\infty = \rho U_\infty^2/2$ is shown in Fig. 4. For blowing, $(p_w)_{\text{rms}}$ increases significantly in the downstream, whereas it decreases for suction. Although the magnitude of blowing velocity is equivalent to that of suction velocity, $(p_w)_{\text{rms}}$ of blowing changes more significantly than that of suction. Because high-amplitude wall pressure fluctuations are linked with streamwise vortices and turbulent kinetic energy production,[10] the activated streamwise vortices and turbulent fluctuations by the wall blowing may cause the increase of $(p_w)_{\text{rms}}$ in the downstream.

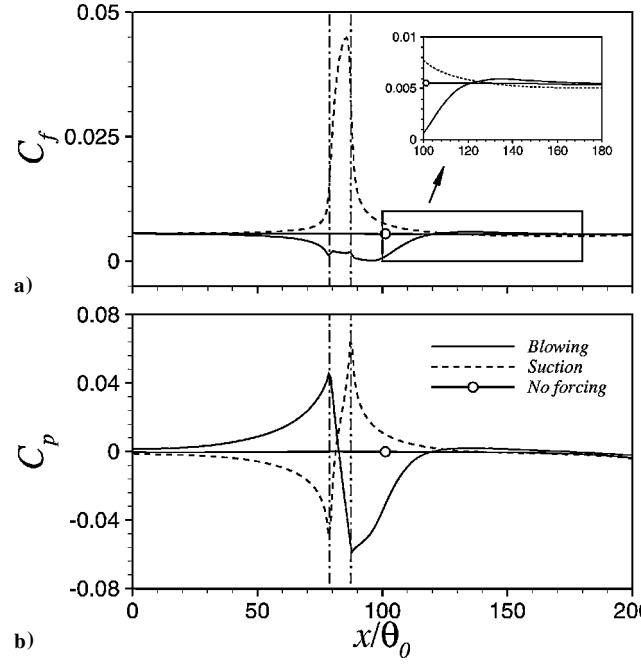

Fig. 3 Streamwise distribution of mean variables at the wall: ---, location of spanwise slot: a) skin-friction coefficient and b) wall pressure coefficient.

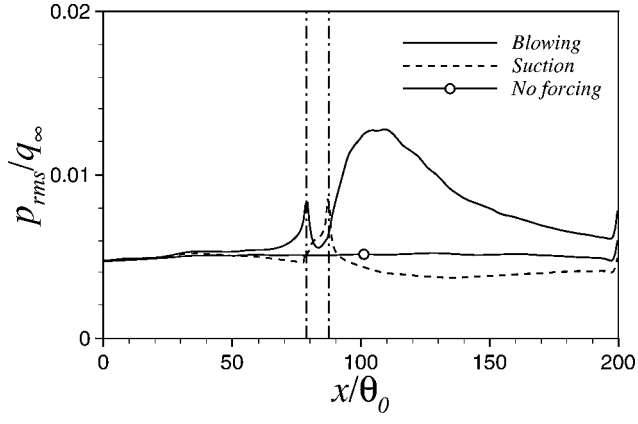

Fig. 4 Streamwise distribution of rms wall pressure fluctuations.

To examine the spectral features of wall pressure fluctuations, the frequency spectra of p_w are obtained using standard techniques for stochastic data.[11] The wall pressure fluctuations $p_w(x, z, t)$ are Fourier transformed in the spanwise direction and time. Let $\hat{p}_w(x, k_z, \omega)$ be the discrete Fourier transform of $p_w(x, z, t)$; then the power spectral density is computed by

$$\Phi(k_z, \omega; x) = \left\langle \hat{p}_w(x, k_z, \omega)\hat{p}^*_w(x, k_z, \omega) \right\rangle \tag{13}$$

where the bracket indicates an average over the spanwise direction and time. The dependence on the streamwise location x is considered from the flow inhomogeneity. The frequency spectra $\phi(\omega; x)$ are obtained by integrating $\Phi(k_z, \omega; x)$ over k_z. All spectra presented in this paper are normalized such that their integral is equal to the mean square of wall pressure fluctuations.

Because of the different characteristics of velocity and length scales, a reliable similarity scaling law is important for the

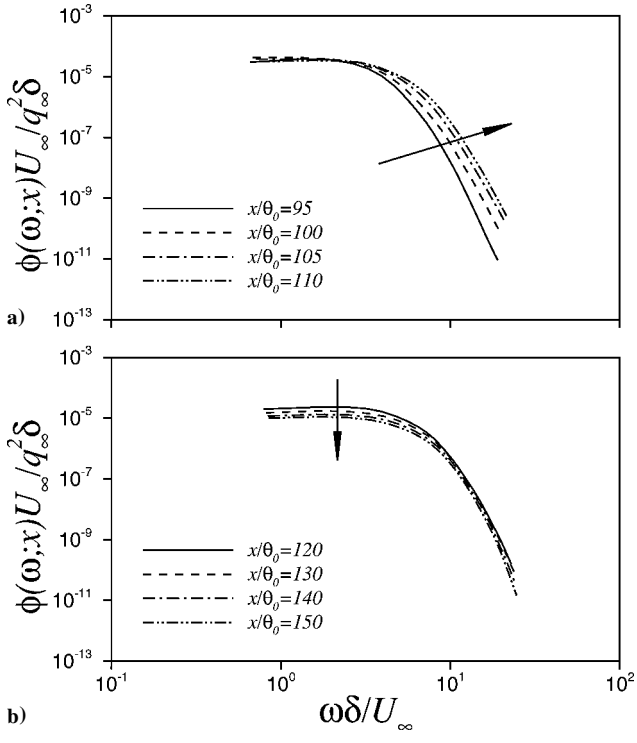

Fig. 5 Frequency spectra of wall pressure fluctuations for blowing: a) near the slot and b) downstream.

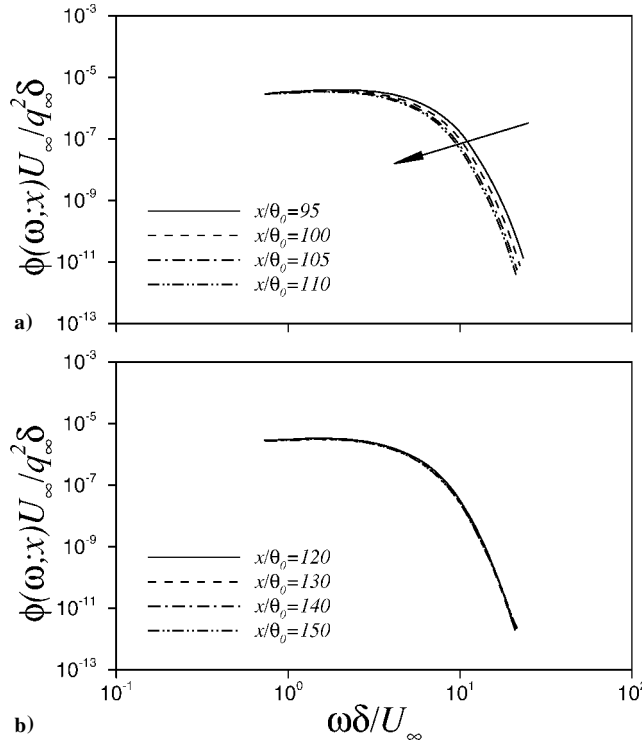

Fig. 6 Frequency spectra of wall pressure fluctuations for suction: a) near the slot and b) downstream.

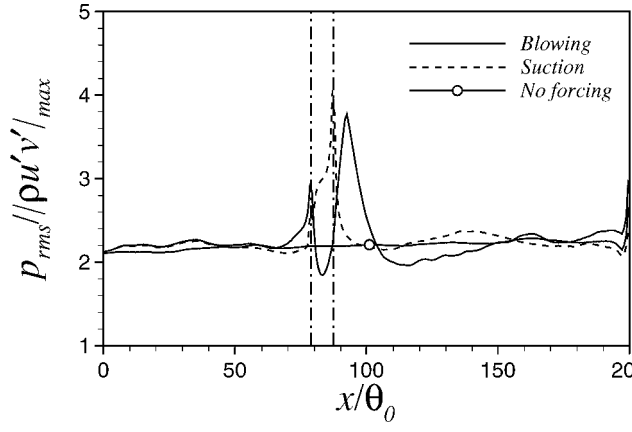

Fig. 7 Streamwise distribution of the rms wall pressure fluctuations.

comparison of frequency spectra. The spectra obtained with the inner variable scaling, not shown in this paper, have a large discrepancy at all frequencies. Any scaling with friction velocity u_τ does not produce collapsed spectra in the presence of pressure gradient. As pointed out by Na and Moin,[11] this is because u_τ is no longer an important parameter in boundary layers with pressure gradient.

The spectra normalized by the outer variables for blowing are shown in Fig. 5. Near the slot $x/\theta_0 < 110$, the spectra seem to collapse in the low frequencies and increase in the high frequencies with increasing the streamwise location x (Fig. 5a). An inspection of Fig. 5a discloses that the power in the high-frequency region has a main role in the increase of $(p_w)_{\rm rms}$ for blowing. In the downstream $x/\theta_0 > 120$, the spectra in the low frequencies decrease with increasing x (Fig. 5b). This means that the decrease of large-scale power gives the decrease of $(p_w)_{\rm rms}$ in the downstream. For suction, the spectra decrease in the high frequencies with increasing x (Fig. 6a), indicating that the decrease of small-scale power produces the decrease of $(p_w)_{\rm rms}$. One could conclude from these spectra that the small scale of wall pressure fluctuations reacts quickly in a short downstream distance to both blowing and suction, whereas the large scale recovers slowly farther downstream.

Figure 7 shows the streamwise distribution of rms wall pressure fluctuations $(p_w)_{\rm rms}$ normalized by the local maximum Reynolds shear stress $|\rho u'v'|_{\rm max}$. Note that there is less variation of wall pressure fluctuations normalized by the local maximum Reynolds shear stress than by the reference dynamic pressure. This means that the maximum Reynolds shear stress $|\rho u'v'|_{\rm max}$ appears to be a better scale to normalize wall pressure fluctuations in a locally forced turbulent boundary layer. This scaling will be further investigated for the frequency power spectra of wall pressure fluctuations. However, the spiky discrepancy due to the nonfluctuating fluid injection is observed near the slot $x/\theta_0 < 100$. The injected fluid through the spanwise slot has zero fluctuations, thereby affecting the velocity fluctuations and the Reynolds shear stress.[15,16]

The frequency spectra normalized by the the maximum Reynolds shear stress $|\rho u'v'|_{\rm max}$ with blowing are presented in Fig. 8. Except near the slot (Fig. 8a), this scaling produces a good collapse of the spectra at all frequencies (Fig. 8b). This means that the local maximum Reynolds shear stress has more direct influence on wall pressure fluctuations. However, the frequency spectra have a large discrepancy near the slot, at which the Reynolds shear stress can be affected by the nonfluctuating injected flow. Overall inspection of Figs. 7 and 8 shows that the Reynolds shear stress $|\rho u'v'|_{\rm max}$ is a better scale to normalize wall pressure fluctuations in a turbulent boundary layer.

B. Two-Point Correlations of Wall Pressure Fluctuations

The spatial characteristics of the wall pressure fluctuations are obtained from the two-point correlations as a function of the streamwise and spanwise spatial separations, which are defined between two locations separated by $(\Delta x, \Delta z)$ as

$$R_{pp}(\Delta x, \Delta z; x) = \frac{\langle p_w(x, z, t) p_w(x + \Delta x, z + \Delta z, t)\rangle}{(p_w)_{\rm rms}(x, z, t)(p_w)_{\rm rms}(x + \Delta x, z + \Delta z, t)} \tag{14}$$

where the bracket indicates an average over the spanwise direction and time. Again, the dependence on the streamwise location x is considered from the flow inhomogeneity. Contour plots of the two-point correlation at four streamwise locations are presented in Fig. 9.

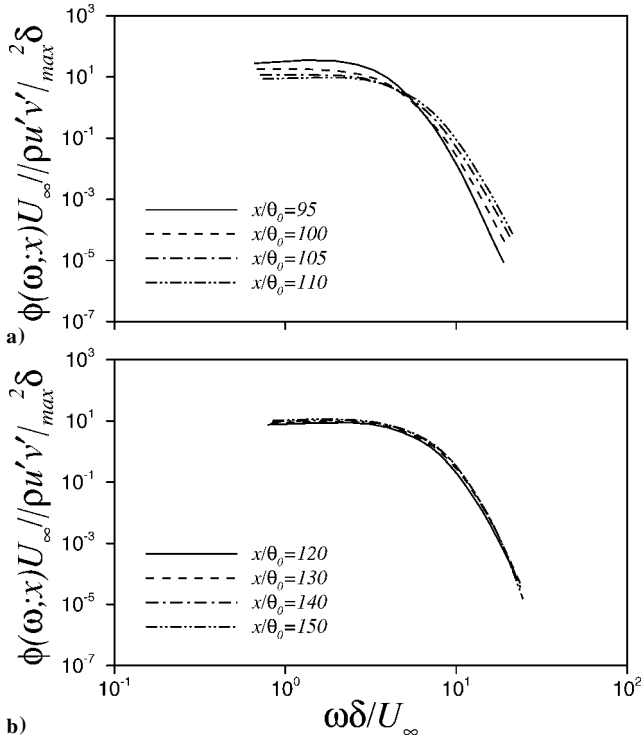

Fig. 8 Frequency spectra of wall pressure fluctuations for blowing: a) near the slot and b) downstream.

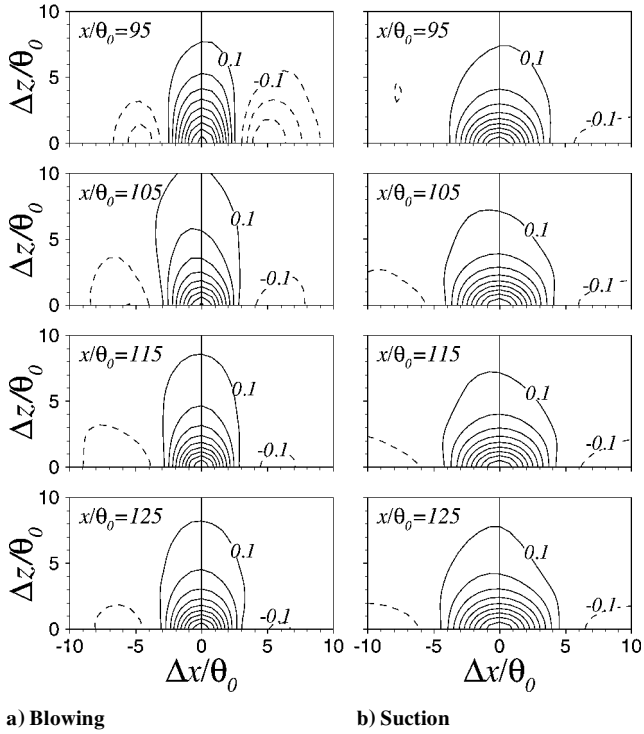

a) Blowing **b) Suction**

Fig. 9 Contour of two-point correlation of wall pressure fluctuations as function of streamwise and spanwise separations; contour levels from −0.3 to 0.9 with 0.1 increment: – – –, negative correlations.

For the purpose of comparison, the spatial separations are normalized by the inlet momentum thickness. For blowing, contours are elongated at larger separations in the spanwise direction (Fig. 9a). The spanwise extent of the widest contour corresponding to the contour level 0.1 increases up to $x/\theta_0 = 105$, at which $(p_w)_{\rm rms}$ has the maximum value. This indicates that the integral length scale of wall pressure fluctuations increases near the slot region. As will be shown next, Sec. III.C, this is due to the strengthened vortical structure,

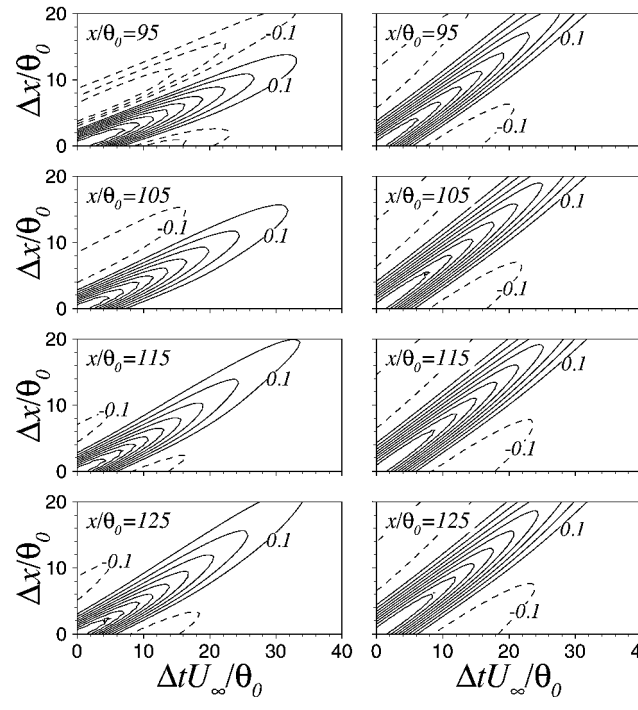

a) Blowing **b) Suction**

Fig. 10 Contour of two-point correlation of wall pressure fluctuations as function of streamwise spatial and temporal separations.

which produces the wall-normal motions in the buffer region and the relevant spanwise spread beneath the viscous sublayer.

Figure 10 shows the two-point correlation of wall pressure fluctuations as a function of the streamwise spatial and temporal separations, which is given by

$$R_{pp}(\Delta x, \Delta t; x) = \frac{\langle p_w(x, z, t) p_w(x + \Delta x, z, t + \Delta t)\rangle}{(p_w)_{\rm rms}(x, z, t)(p_w)_{\rm rms}(x + \Delta x, z, t + \Delta t)} \tag{15}$$

where the bracket indicates an average over the spanwise direction and time. The strong convective nature of the wall pressure fluctuations is seen by the concentration of the contours in a band. A slight increase in the slope of $\Delta x^+/\Delta t^+$ indicates that the convection velocity of large eddies is higher than that of small eddies. Furthermore, the slope of the contour with blowing increases with increasing the streamwise location x (Fig. 10a), whereas it has little change with suction (Fig. 10b). This means that the convection velocities of the wall pressure fluctuations increase with increasing x near the slot region for blowing.

C. Analysis of Pressure Source Terms

Poisson's equation for pressure fluctuations is derived by taking the divergence of Eq. (1). When the velocity field is decomposed into mean and fluctuations as $u_i = U_i + u_i'$, the equation can be written as

$$\frac{\partial^2 p}{\partial x_i \partial x_i} = -\left\{ 2\frac{\partial U_i}{\partial x_j}\frac{\partial u_j'}{\partial x_i} + \frac{\partial^2}{\partial x_i \partial x_j}(u_i'u_j' - \overline{u_i'u_j'}) \right\} \tag{16}$$

where x_i are the Cartesian coordinates, u_i are the corresponding velocity components, and the overbar indicates an average over the spanwise direction and time. The first term on the right-hand side is the mean shear (MS) source term (linear or rapid), whereas the other term represents the sum of the turbulence–turbulence (TT) source term (nonlinear or slow). The MS and TT terms are given by

$$T^{\rm MS} = 2\frac{\partial U_i}{\partial x_j}\frac{\partial u_j'}{\partial x_i} \tag{17}$$

$$T^{\mathrm{TT}} = \frac{\partial^2}{\partial x_i \partial x_j}(u_i' u_j' - \overline{u_i' u_j'}) \tag{18}$$

For the present boundary layer, the spanwise mean velocity gradient is zero. Among the linear source terms T^{MS}, $2(\partial U/\partial y)(\partial v'/\partial x)$ is about 50–100 times larger than any other MS terms. The TT source terms can be written as

$$T_{11}^{\mathrm{TT}} = \left(\frac{\partial u'}{\partial x}\right)^2 - \frac{\partial^2}{\partial x^2}\overline{u'^2} \tag{19}$$

$$T_{12}^{\mathrm{TT}} = T_{21}^{\mathrm{TT}} = \frac{\partial v'}{\partial x}\frac{\partial u'}{\partial y} - \frac{\partial^2}{\partial x \partial y}\overline{u'v'} \tag{20}$$

$$T_{13}^{\mathrm{TT}} = T_{31}^{\mathrm{TT}} = \frac{\partial w'}{\partial x}\frac{\partial u'}{\partial z} \tag{21}$$

$$T_{22}^{\mathrm{TT}} = \left(\frac{\partial v'}{\partial y}\right)^2 - \frac{\partial^2}{\partial y^2}\overline{v'^2} \tag{22}$$

$$T_{23}^{\mathrm{TT}} = T_{32}^{\mathrm{TT}} = \frac{\partial w'}{\partial y}\frac{\partial v'}{\partial z} \tag{23}$$

$$T_{33}^{\mathrm{TT}} = \left(\frac{\partial w'}{\partial z}\right)^2 \tag{24}$$

where x, y, and z are the Cartesian coordinates and u, v, and w are the corresponding velocity components, respectively.

Contours of the rms source terms from Eqs. (19) and (20) are shown in Fig. 11. For both blowing (Fig. 11a) and suction (Fig. 11b), rms of the nonlinear source term T^{TT} is much larger than that of the linear source term T^{MS} throughout the boundary layer. This is because $\partial u_j'/\partial x_i$ is rather small in the present turbulent boundary layer with blowing or suction. Furthermore, the rms source terms are more activated by blowing (Fig. 11a) than by suction (Fig. 11b), even though the velocities of blowing or suction are the same. This means that the pressure source terms of Poisson's equation are more affected by blowing than by suction.

To obtain further insight of the nonlinear source term T^{TT}, the profiles of the nonlinear source terms for blowing or suction are shown in Fig. 12. For comparison, the difference between the rms source term for blowing or suction and the term without blowing or suction is presented. For bowing (Fig. 12a), $T_{23}^{\mathrm{TT}} = (\partial v'/\partial z)(\partial w'/\partial y)$ has the largest rms value near $y^+ = 20$, which corresponds to the average location of the center of streamwise vortices. Note that $T_{22}^{\mathrm{TT}} \cong (\partial v'/\partial y)^2$ has the largest value in the viscous sublayer near $y^+ = 5$, which would be related to the wall-normal motions such as sweep or ejection. A closer inspection of Fig. 12 indicates that the second largest term in the viscous sublayer is $T_{33}^{\mathrm{TT}} = (\partial w'/\partial z)^2$, which is due to a high spanwise gradient as the flow spreads out. In summary, the activated streamwise vortices and the relevant motions

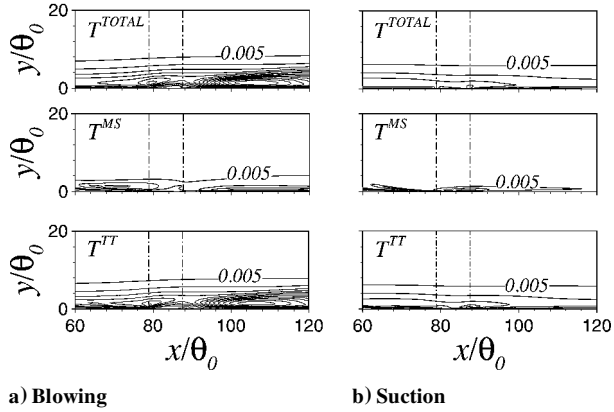

Fig. 11 Contours of rms source terms; contour levels from 0.005 to 0.07 with 0.005 increment.

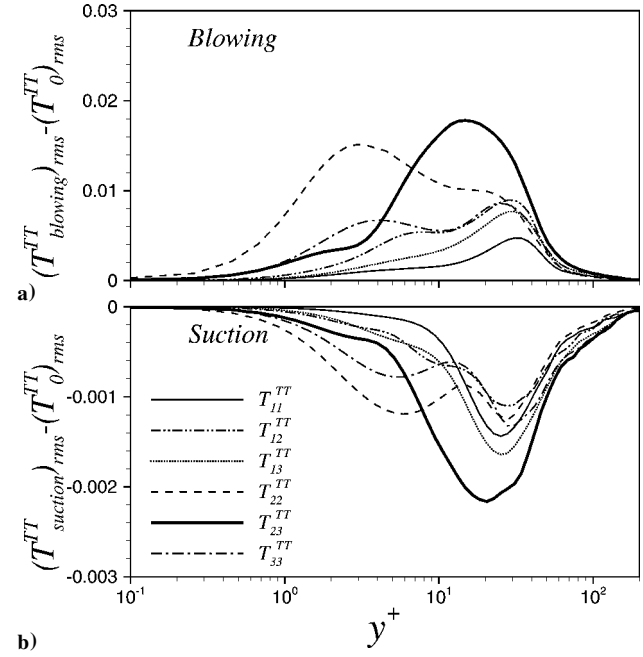

Fig. 12 Profiles of rms TT terms.

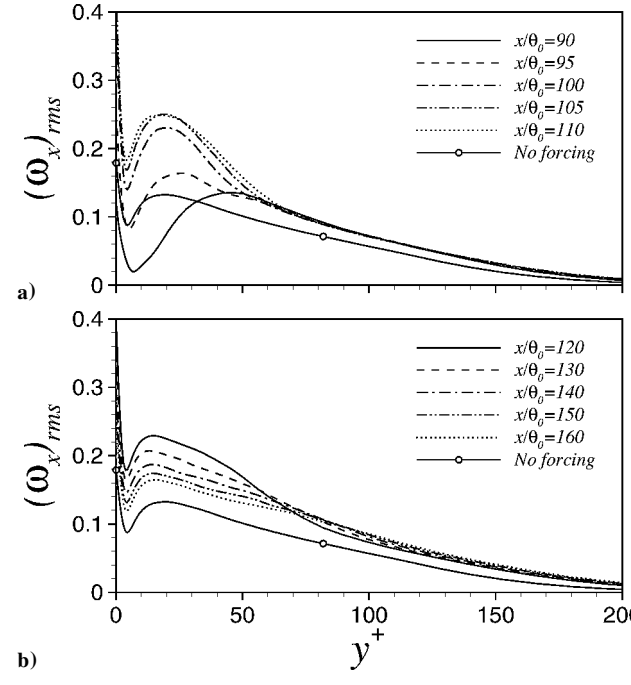

Fig. 13 Variations of rms streamwise vorticity fluctuations for blowing: a) near the slot and b) downstream.

in the viscous sublayer are responsible for the increase of wall pressure fluctuations and the generation of large-elongated structures. On the other hand, when uniform suction is applied, the strength of the rms source terms are weakened. Note that the difference of the source terms for blowing (Fig. 12a) is about 10 times larger than that for suction (Fig. 12b). This means that the pressure source terms are 10 times more affected by blowing than by suction for the same blowing or suction velocities.

Figure 13 shows the variations of rms streamwise vorticity fluctuations ω_x for blowing. Note that the strength of ω_x for blowing is stronger than that without blowing, whereas the strength for suction is weaker (Fig. 14). For blowing, the local maximum location of ω_x moves away from the wall near the slot $x/\theta_0 < 110$ (Fig. 13a), indicating that the quasi-streamwise vortices are lifted up. Hence, the magnitude of ω_x increases significantly and has the maximum value at $x/\theta_0 = 110$, at which $(p_w)_{\mathrm{rms}}$ has the maximum value. This

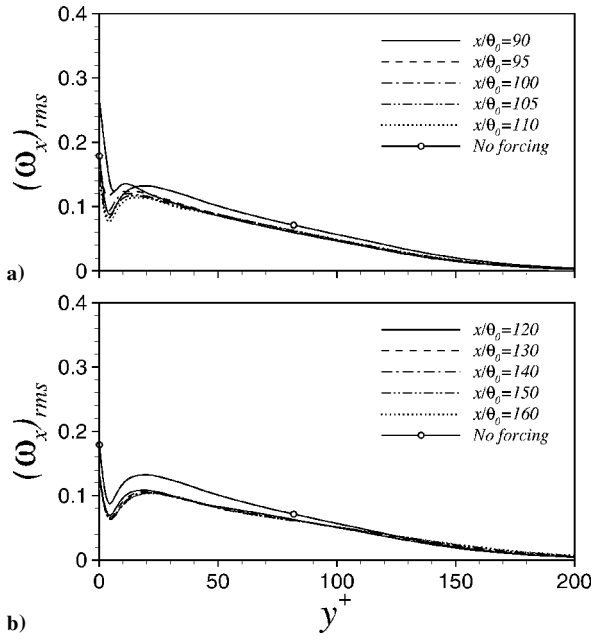

Fig. 14 Variations of rms streamwise vorticity fluctuations for suction: a) near the slot and b) downstream.

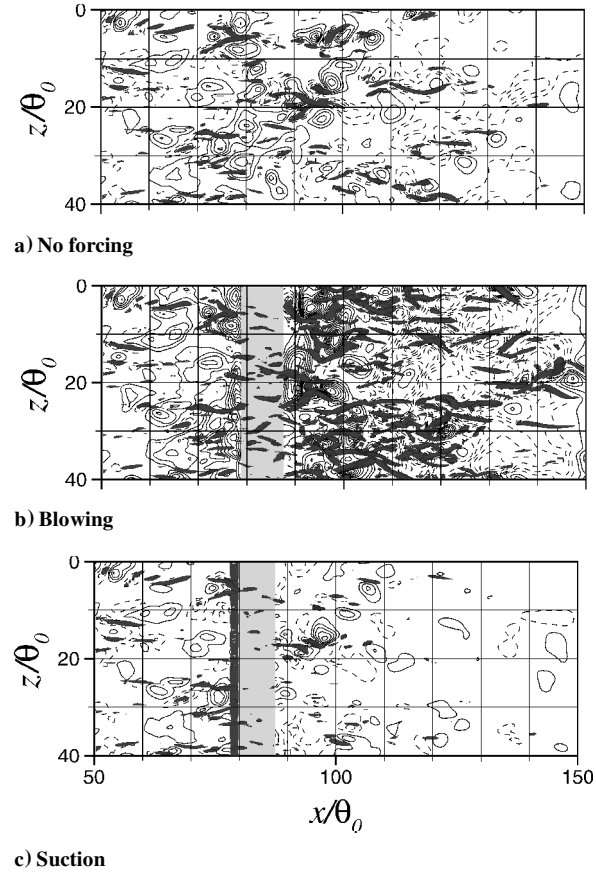

Fig. 15 Wall pressure fluctuations and corresponding streamwise vortices: – – –, negative wall pressure fluctuations; contour levels from −0.07 to 0.07 with 0.05 increment.

suggests that the magnitude of the nonlinear source term T_{23}^{TT}, which is related to ω_x, increases in the vicinity of the wall, thereby affecting the increase of wall pressure fluctuations.

Finally, the contours of wall pressure fluctuations and associated streamwise vortices are shown in Fig. 15 for blowing and suction. The vortex identification method proposed by Jeong and Hussain[20] is employed, which is based on the detection of local pressure minima caused by vortex cores. The isosurfaces of the second largest eigenvalue of the tensor $S^2 + \Omega^2$ are plotted, where S and Ω are the symmetric and antisymmetric parts of the velocity gradient tensor.[20] It is seen that the regions of high wall pressure fluctuations are associated with the strong streamwise vortices in the vicinity of the wall. However, weak wall pressure fluctuations occur beneath the regions where a passage of streamwise vortices is rare. As pointed out by Kim et al.,[10] this is because the rise of high wall pressure fluctuations coincides with the passage of streamwise vortices. The sweep sides of the streamwise vortices are directly above the regions of positive wall pressure fluctuations, whereas negative wall pressure fluctuations are found to occur beneath the ejection sides or the cores of the streamwise vortices.[10] The activated streawise vortices for blowing play a main role in the increase of wall pressure fluctuations, whereas the suction diminishs turbulent fluctuations.

IV. Conclusions

A detailed numerical analysis has been performed to delineate the characteristics of wall pressure fluctuations in a turbulent boundary layer with uniform blowing or suction. The statistical descriptions of wall pressure fluctuations were obtained by performing a DNS of a spatially developing turbulent boundary layer. When uniform bowing is applied from a spanwise slot, lifted and strengthened quasi-streawise vortices paly a main role in the increase of the magnitude of the nonlinear source terms in Poisson's equation. In particular, T_{23}^{TT} increases in the buffer region, which is related to ω_x, whereas the T_{22}^{TT} and T_{33}^{TT} terms increase in the viscous sublayer because of the relevant resulting motions beneath the vortices. The opposite is observed for suction. The increasing rate by blowing is of the order of about 10 times larger than the decreasing rate by suction. Although the magnitude of blowing velocity is equal to that of suction velocity, $(p_w)_{rms}$ of blowing changes more significantly than that of suction. Because of the relevant motions beneath quasi-streamwise vortices, the large elongated structure of wall pressure fluctuations is observed near the maximum location of $(p_w)_{rms}$ for blowing. For both blowing and suction, the small scale of wall pressure fluctuations reacts in a short downstream distance to the spanwise slot, whereas the large scale recovers farther downstream. The Reynolds shear stress $|\rho u' v'|_{max}$ is a better scale to normalize wall pressure fluctuations.

Acknowledgments

This research was supported by a grant from the National Research Laboratory of the Ministry of Science and Technology, Republic of Korea. Partial support from the Underwater Acoustics Research Center of the Agency for Defense Development is acknowledged.

References

[1]Blake, W. K., *Mechanics of Flow-Induced Sound and Vibration*, Academic Press, New York, 1986, pp. 497–588.

[2]Willmarth, W. W., "Wall Pressure Fluctuations in a Turbulent Boundary Layer," *Journal of the Acoustical Society of America*, Vol. 28, 1958, pp. 1048–1053.

[3]Bull, M. K., "Wall Pressure Fluctuations Associated with Subsonic Turbulent Boundary Layer Flow," *Journal of Fluid Mechanics*, Vol. 28, 1967, pp. 719–754.

[4]Willmarth, W. W., "Pressure Fluctuations Beneath Turbulent Boundary Layers," *Annual Review of Fluid Mechanics*, Vol. 7, 1975, pp. 13–38.

[5]Choi, H., and Moin, P., "On the Space–Time Characteristics of Wall-Pressure Fluctuations," *Physics of Fluids*, Vol. A2, No. 8, 1990, pp. 1450–1460.

[6]Lee, I., and Sung, H. J., "Development of an Array of Pressure Sensors with PVDF Film," *Experiments in Fluids*, Vol. 26, 1999, pp. 27–35.

[7]Thomas, A. S. W., and Bull, M. K., "On the Role of Wall Pressure Fluctuations in Deterministic Motions in the Turbulent Boundary Layer," *Journal of Fluid Mechanics*, Vol. 128, 1983, pp. 283–322.

[8]Johansson, A. V., Her, J.-Y., and Haritonidis, J. H., "On the Generation of High-Amplitude Wall-Pressure Peaks in Turbulent Boundary Layers and Spots," *Journal of Fluid Mechanics*, Vol. 175, 1987, pp. 119–142.

[9]Kim, J., "On the Structure of Pressure Fluctuations in Simulated Turbulent Channel Flow," *Journal of Fluid Mechanics*, Vol. 205, 1989, pp. 421–451.

[10]Kim, J., Choi, J.-I., and Sung, H. J., "Relationship Between Wall Pressure Fluctuations and Streamwise Vortices in a Turbulent Boundary Layer," *Physics of Fluids*, Vol. 14, 2002, pp. 898–901.

[11]Na, Y., and Moin, P., "The Structure of Wall-Pressure Fluctuations in Turbulent Boundary Layers with Adverse Pressure Gradient and Separation," *Journal of Fluid Mechanics*, Vol. 377, 1998, pp. 347–373.

[12]Lee, I., and Sung, H. J., "Characteristics of Wall Pressure Fluctuations in Separated and Reattaching Flows over a Backward-Facing Step: Part II. Unsteady Wavelet Analysis," *Experiments in Fluids*, Vol. 30, 2001, pp. 273–282.

[13]Lee, I., and Sung, H. J., "Multiple-Arrayed Pressure Measurement Toward the Investigation of the Unsteady Flow Structure of a Reattaching Shear Layer over a Backward-Facing Step," *Journal of Fluid Mechanics*, Vol. 463, 2002, pp. 377–402.

[14]Chung, Y. M., and Sung, H. J., "Initial Relaxation of Spatially-Evolving Turbulent Channel Flow Subjected to Sudden Wall Blowing and Suction," *AIAA Journal*, Vol. 39, 2001, pp. 2091–2099.

[15]Park, J., and Choi, H., "Effects of Uniform Blowing or Suction from a Spanwise Slot on a Turbulent Boundary Layer Flow," *Physics of Fluids*, Vol. 11, 1999, pp. 3095–3105.

[16]Kim, K., Sung, H. J., and Chung, M. K., "Assessment of Local Blowing and Suction in a Turbulent Boundary Layer," *AIAA Journal*, Vol. 40, 2002, pp. 175–177.

[17]Kim, K., Baek, S.-J., and Sung, H. J., "An Implicit Velocity Decoupling Procedure for the Incompressible Navier–Stokes Equations," *International Journal for Numerical Methods in Fluids*, Vol. 38, 2002, pp. 125–138.

[18]Lund, T. S., Wu, X., and Squires, K. D., "Generation of Turbulent Inflow Data for Spatially-Developing Boundary Layer Simulations," *Journal of Computational Physics*, Vol. 140, 1998, pp. 233–258.

[19]Spalart, P. R., "Direct Numerical Simulation of a Turbulent Boundary Layer up to $Re_\theta = 1410$," *Journal of Fluid Mechanics*, Vol. 187, 1988, pp. 61–98.

[20]Jeong, J., and Hussain, F., "On the Identification of a Vortex," *Journal of Fluid Mechanics*, Vol. 285, 1995, pp. 69–94.

P. Givi
Associate Editor